ADVANCED ELECTRONIC MATERIALS Open Access
www.advelectronicmat.de

Enhanced Thermoelectric Performance of MnTe by Decoupling of Electrical and Thermal Transports

Abdul Basit, Jiwu Xin, Yubo Luo, Ji-Yan Y. Dai, and Junyou Yang**

Lead-free polycrystalline manganese telluride holds great potential in the development of waste heat recovery due to its fascinating physical properties. However, the poor thermoelectric (TE) performance in the p-type MnTe alloys always results from their inferior carrier concentration, leading to low power factor and high thermal conductivity which restrict the overall thermoelectric performance. In this work, the problem is solved by decoupling its electrical and thermal transports through the hole donor Ge-deficiency in MnTe + *x* mol.% GeTe ($0 \leq x \leq 4$) compounds. Intrinsically, extra GeTe in MnTe + *x* mol.% GeTe compound offers free charge carriers due to a narrow bandgap comparatively, realizing not only a full assessment of stimulated electrical performance but also an enhanced power factor. Moreover, benefiting from the nano-precipitates and tweed microstructures, the lattice thermal conductivity effectively reduces due to the intensive phonon scattering accordingly. Ultimately, a maximum ZT of ≈1.2 at 873 K in the 3 mol.% GeTe doped MnTe sample is realized.

1. Introduction

Owing to the increasing demand for energy devices and a dramatic escalation of fossil fuels, thermoelectric (TE) materials have demonstrated a large range of potential applications in power generation and thermal cycling with high scalability,[10,28,43,45] leading to the environmental impact of a sustainable global climate. In general, the major restriction to TE materials' large-scale applications is inferior conversion efficiency as characterized by the figure of merit $ZT = S^2\sigma T/\kappa$. Optimizing an ideal TE material and scaling a higher conversion efficiency requires an enhanced Seebeck coefficient (S) and electrical conductivity (σ), while in the meantime, suppressed thermal conductivity (κ) is needed.[12,23] In this scenario, a variety of strategies such as band structure engineering and energy filtering approaches have been adopted to optimize the power factor;[12,49,58,68] while more specifically, a synergistic nano-structuring has been proposed to reduce the thermal conductivity[30,55] in skutterudites,[51] clathrates,[35] half-Heusler[41] and Zintl-phases[20] etc. Moreover, entropy engineering has also been adopted to manipulate and stabilize the TE materials with high symmetries, and thus the thermal conductivities are reduced by the mass fluctuation and point defects, etc.[18,39,66] Therefore, the challenging counterparts electrical and thermal transports properties in thermoelectric materials have been successfully decoupled to attain significant ZT in some compounds i.e; PbTe,[9,15,48,63] $AgMnGeSbTe_4$,[34] PbSe,[65] GeTe,[19,54] $AgSbTe_2$,[32,40] Cu_2Se,[24,61,64] SnSe,[27,31,44,53] and $CuInTe_2$.[17,25,52]

During searching for green, non-toxic, and large-scale thermoelectric materials, manganese chalcogenides have gained much attention recently, among them, MnTe is a typical chalcogenide possessing a hexagonal (NiAs) crystal structure and a space group P63/mmc.[42,47] Referring to the literature, high carrier concentration and reduced thermal conductivity are associated with the development of new thermoelectric materials, thus, doping of various compositions in MnTe is preferred to obtain high TE performance in MnTe-based compounds. However, the wide bandgap (≈0.82 eV), and inferior intrinsic carrier concentration ($\approx 10^{18}$ cm^{-3}) have always restricted a significant thermoelectric performance in MnTe compounds.[2–4,11,26] Some reports have revealed the regulation of thermoelectric properties in MnTe-based compounds, for example, the inferior ZT of 0.41 was realized from the enhanced power factor $\approx 0.414 \times 10^{-3}$ W mK^{-2} at 773 K in $Mn_{0.51}Te_{0.49}$ compound without deteriorating the lattice thermal conductivity.[22] Further, the cation doping of sulfur and copper was employed in Te and Mn sites to regulate the carrier concentration in the MnTe compound separately, resulting in increased ZTs of 0.65 and 0.55 in $MnTe_{0.9}S_{0.1}$ and $Mn_{0.925}Cu_{0.075}Te$

A. Basit, J.-Y. Y. Dai
Department of Applied Physics
The Hong Kong Polytechnic University
Kowloon 999077, Hong Kong
E-mail: jiyan.dai@polyu.edu.hk

J. Xin
School of Electrical and Electronic Engineering
Nanyang Technological University
50 Nanyang Ave, Singapore 639798, Singapore

Y. Luo, J. Yang
State Key Laboratory of Material Processing & Die Mold Technology
Huazhong University of Science and Technology
Wuhan 430074, China
E-mail: jyyang@mail.hust.edu.cn

The ORCID identification number(s) for the author(s) of this article can be found under https://doi.org/10.1002/aelm.202300809

DOI: 10.1002/aelm.202300809

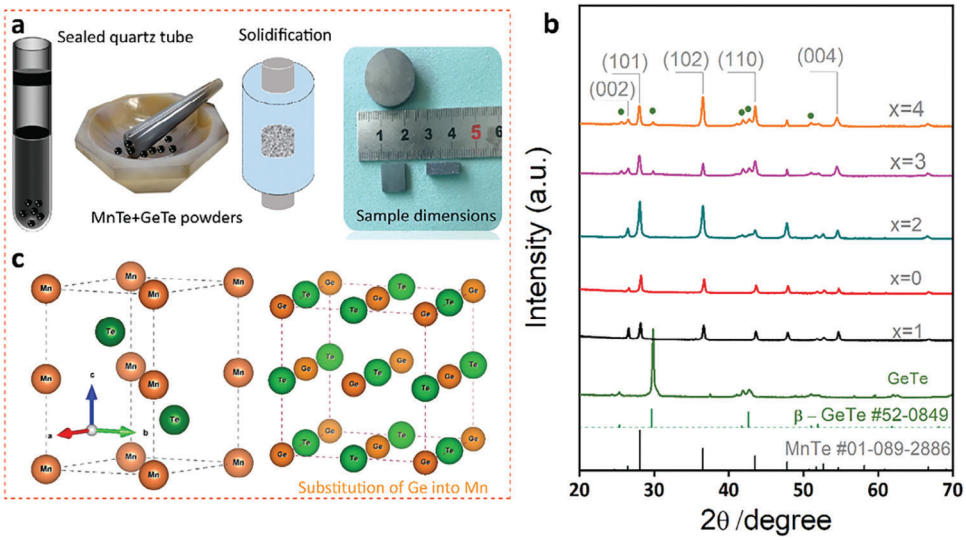

Figure 1. a) Schematic illustration of the preparation of MnTe + *x* mol.% GeTe ($0 \le x \le 4$); b) powder XRD diffraction patterns of MnTe + *x* mol.% GeTe ($0 \le x \le 4$); c) representation for the replacement process of Mn by Ge-site.

samples, respectively.[37,56] In addition to the optimized electrical performance, a significant increase in power factor was also reported from stimulated holes in pristine MnTe from the incorporated Na and Ag into the Mn-site.[60] Another report reveals the addition of Na_2S in the MnTe compound facilitating the carrier density along with a greatly reduced thermal conductivity, hence resulting in an enlarged ZT of 1.09 at 873 K.[38] Recently, significant transport properties in MnTe-based compounds were reported with the effect of co-doping Li, Na, and K, through which the ZT up to 0.93, 1.09, and 1.3 at 873 K, respectively have been reached.[57] Though the above-mentioned progress has been realized, the doping of volatile metals may bring reliability issues due to the high diffusivity of those metal ions. Besides, Jinfeng et al. employed Se and Na into MnTe by a facile and SPS process separately and reported a maximum ZT of 1.03 at 873 K due to the suppression of lattice thermal conductivity (0.56 W/mK) of $MnTe_{0.92}Se_{0.08}$.[7] However, the carrier concentration of MnTe was tuned through enhancement in density-of-state effective mass by Na that resulted in a high power factor ≈900 $\mu W m^{-1} K^{-2}$ at 873 K.[8] Familiar with the drawback of inferior carrier concentration, Yiyuan et al. realized an impressive ZT ≈1.3 in $Mn_{0.96}Ge_{0.04}Sb_2Te_4$ at 873 K due to the effective increase in carrier mobility, however, the corresponding single-stage generated module led to the efficiency of 4.6% at temperature gradient 480 K.[29] Furthermore, the development of moderate thermoelectric applications in MnTe compounds is still rather inferior compared to other state-of-the-art telluride TE compounds.[46]

Intuitively, GeTe is a degenerate semi-conductor possessing an extremely high intrinsic hole density of ≈3.6×10^{21} cm^{-3} coming from the extensive Ge deficiency.[5,36] Considering the lower bandgap and higher carrier concentration of GeTe comparatively to pristine MnTe, the doping approach could be an effective route in boosting the TE performance of MnTe. This work reveals the development in TE properties of MnTe from the optimized carriers and mobility and overcomes the hindrance in the Seebeck coefficient owing to the hole donor Ge-deficiency. Also, the residual GeTe nano-precipitates effectively suppress the thermal conductivities and thus improve the ZT up to ≈1.2 at 873 K in a 3 mol.% GeTe doped MnTe.

2. Results and Discussion

2.1. Phase and Microstructure of MnTe + *x* mol.% GeTe ($0 \le x \le 4$)

XRD diffraction patterns from the prepared GeTe and the hot-pressed MnTe + *x* mol.% GeTe bulk samples are shown in **Figure 1b**. For XRD patterns of the $x \le 1$ sample, all the reflection peaks can be indexed based on the hexagonal structure of MnTe with a space group P63/mmc (PDF# 01–089–2886). Extra peaks of GeTe (PDF# 52–0849) can be detected in the patterns of samples with $x > 1$, indicating the existence of a GeTe secondary phase in these samples. The single phase of pure MnTe suggests that Ge can easily be substituted to the Mn-site by the hot-press process as noticed in Figure 1c. However, GeTe crystallizes as a secondary phase in the matrix of MnTe at high content and will be introduced in the following sections.

To analyze the microstructure of the GeTe-doped MnTe samples, FE-SEM observations and EDX analysis were carried out and presented in **Figure 2**, where Figure 2a–c represents the fractographs with the $x = 1$, 2, and 3 mol.% GeTe added MnTe samples, respectively. The fractographs of the samples show their good crystallinity and EDX composition analyses to the corresponding marked points also show consistency with the nominal compositions in Figure 2d–f. Figure 2g demonstrates some secondary phases of layer-structured GeTe in the marked circles, while the enlarged image of a typical GeTe crystal structure in the rectangular area of Figure 2c was also reported in some other works.[13,14,50] Furthermore, EDX mapping (Figure 2h–j) for the area of Figure 2g shows that this area is (Ge, Te)-rich and Mn-poor in composition indicating its nature of GeTe precipitation, as presented in Figure 2h,i.

To further characterize the microstructure of the 3 mol.% GeTe doped sample, TEM characterization was carried out and the

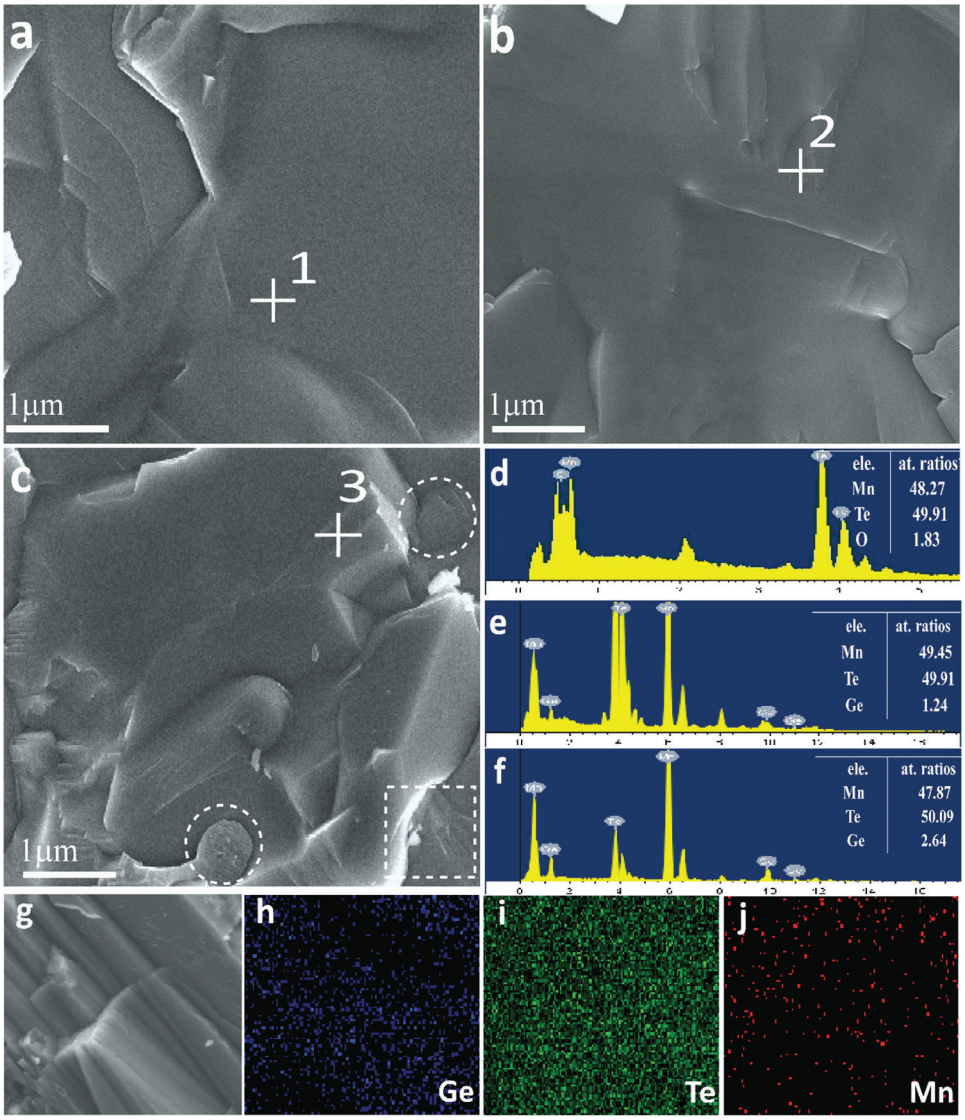

Figure 2. FE-SEM fractographs of the MnTe with a) $x = 1\%$GeTe; b) $x = 2\%$GeTe; c) $x = 3\%$GeTe respectively; d-f) EDS of the marked points in Figure 2a–c respectively; g) enlarged fractograph of the rectangular area in Figure 2c; h–j) corresponding mapping of the morphology in Figure 2g.

results are presented in **Figure** 3a. As illustrated in Figure 3b there are some lamellar structures in the matrix with widths of 50–100 nm; these streaks are attributed to GeTe precipitates resulting from the high content of GeTe in MnTe. HRTEM image (shown in Figure 3c) of the rectangular area (A) indicated in Figure 3b reveals the cubic structure of GeTe by the corresponding lattice plane of (111). One can also clearly see the tweed-structured (like Moiré fringes circled in Figure 3c) nano-regions presented in the GeTe metrics which may result from structural or elemental modulation; these nano-regions act as phonon scattering source, leading to reduced thermal conductivity. Figure 3d presents the HRTEM image of the selected area (B) in Figure 3b, where the lattice spacing of (102) for hexagonal and (200) for cubic correspond to the well-matched planes with XRD data of MnTe and GeTe, respectively. In addition, we conducted strain analysis alongside geometric phase analysis (GPA) using the HRTEM image (Figure 3e). The inverse FFT image (see inset Figure 3e) revealed an inhomogeneous stain distribution with aligned strain centers which can be observed in the tensor map (Figure 3f) representing the ϵ_{xx} to ϵ_{yy} directions. This result suggests that the incorporation of GeTe induces elastic strain and results in a wide scattering effect on acoustic phonons.

2.2. Thermoelectric Performance of MnTe + *x* mol.% GeTe ($0 \leq x \leq 4$)

Figure 4 presents temperature-dependent electrical transport properties of the hot-pressed MnTe + *x* mol.% GeTe ($0 \leq x \leq 4$) samples. At room temperature, the carrier density and mobility for the MnTe + *x* mol.% GeTe ($0 \leq x \leq 4$) samples demonstrate the increasing trend of carrier concentration with the addition of GeTe content resulting from the effective high hole Ge deficiency (Figure S3, Supporting Information). As shown in

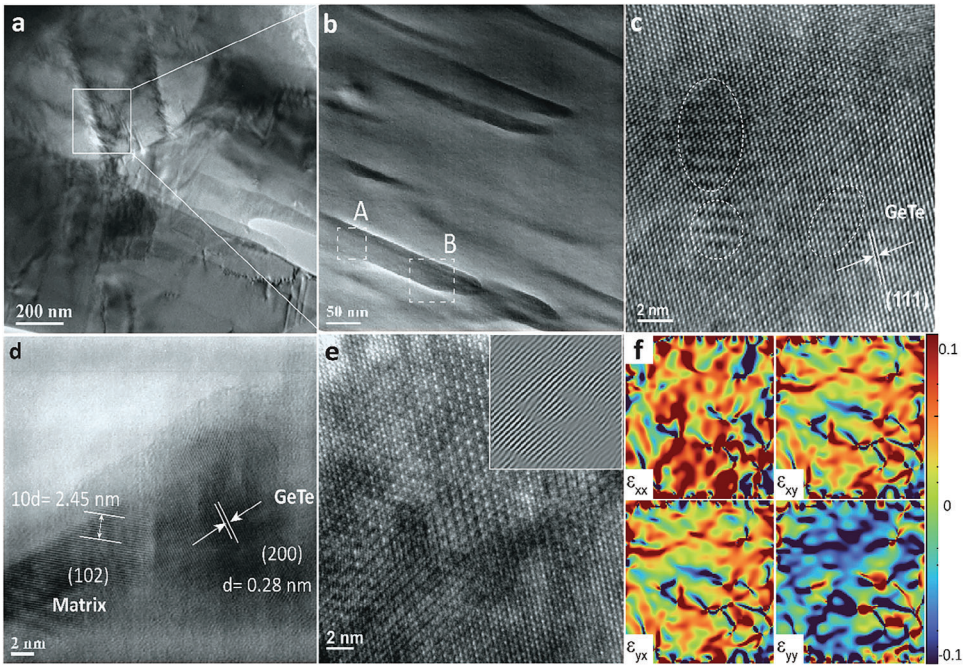

Figure 3. a) TEM micrograph of the sample with the addition of 3 mol.% GeTe; b) enlarged TEM image in Figure 3a; c) TEM image of area A in Figure 3b; d) HRTEM of area B in Figure 3b; e) HRTEM of 3 mol.% GeTe added MnTe and corresponding inverse FFT image (inset of Figure 3e); and f) GPA analysis along the (i) ϵ_{xx}, (ii) ϵ_{xy}, (iii) ϵ_{yx} and (iv) ϵ_{yy} directions.

Figure 4a, this characteristic can further decrease the electrical resistivity sharply for all the GeTe-doped MnTe samples at higher temperatures. It suggests that a higher GeTe content led to high carrier concentration and thus significant reduction in electrical resistivity of MnTe-compounds has been attained which can be attributed to the thermal excitation with increasing temperatures. In addition, the deviation of carrier concentration in x = 4% mol.% GeTe sample suggests that Ge may not be easily added into the site of Mn as ascribed by the over-solubility limit (Figure S3, Supporting Information), and thus the electrical resistivity slightly increases as compared to the other samples. By contrast, carrier mobility decreases with increased GeTe amount (Table S1, Supporting Information); this can be attributed to the electronegativity differences of Mn, Ge, and Te that facilitate the scattering effect of point defects. For instance, as observed in some previous works,[3,38,57] a constant increase in the peaks of electrical resistivity for all the MnTe + x mol.% GeTe ($0 \leq x \leq 4$) samples reveal the intrinsic bi-polar nature of MnTe at 410 K.[1,47] Likewise, as shown in Figure 4b, the Seebeck coefficient for all the MnTe + x mol.% GeTe ($0 \leq x \leq 4$) samples also decrease with the increased carrier concentration at the entire range of temperatures. It should be noticed that all the samples exhibit positive Seebeck coefficients, demonstrating the *p*-type nature of all samples. However, the increased amount of GeTe in the pristine MnTe results in degenerate characteristics at elevated temperatures. Such features elucidate that employed GeTe has a vital role in the electrical transport properties of MnTe. In addition, as given in Figure 4c, the estimated Pisarenko curve for the Seebeck coefficients and carrier densities (n_H) also reveals a similar trend to the calculated S which is close to the experimental values. The major limitation to the high electrical resistivity of pristine MnTe has been substantially revealed with effective optimization of the Seebeck coefficient in MnTe + x mol.% GeTe ($0 \leq x \leq 4$) samples, resulting in an improved power factor of 3 mol.% GeTe added MnTe at 873 K which is 91% higher than that of pristine MnTe as shown in Figure 4d.

Temperature-dependent total thermal conductivity (κ) and lattice thermal conductivity (κ_l) for MnTe + x mol.% GeTe ($0 \leq x \leq 4$) samples are presented in **Figure 5**. One can see that the thermal conductivities of samples decrease with the increased temperature due to the GeTe influence. Whereas the propagation of heat-carrying phonons results in a substantial decrease of thermal transport specifically for x = 4 mol.% GeTe sample (see Figure 5a). Generally, the reduction in thermal conductivities can be ascribed to the decreasing behaviors of thermal diffusivity in MnTe-based materials owing to the mass fluctuations with the doping content at elevated temperatures.[16] Here, the obvious decreasing trend in thermal transport is consistent with the electrical resistivity and Seebeck coefficient governed by the addition of GeTe content. Such behavior suggests the scattering of high-frequency phonons to the boundaries of the matrix and other phases and thus facilitates the reduction in thermal conductivities[59,62] due to the possible planar defects as discussed in Figure 3b. In this work, total thermal conductivities (κ) have been reduced effectively and the lattice thermal conductivities were obtained by subtracting electronic thermal conductivities (κ_e) from κ (Figure S4, Supporting Information) using the Wiedemann–Franz law $\kappa_e = L\sigma T$.[33] However, the planar defects might not be sufficient to facilitate the suppressed lattice thermal conductivity with a small content of GeTe in the MnTe as shown in Figure 5b. Besides, some observed lamella nano precipitates and other planar defects originating from the high GeTe content

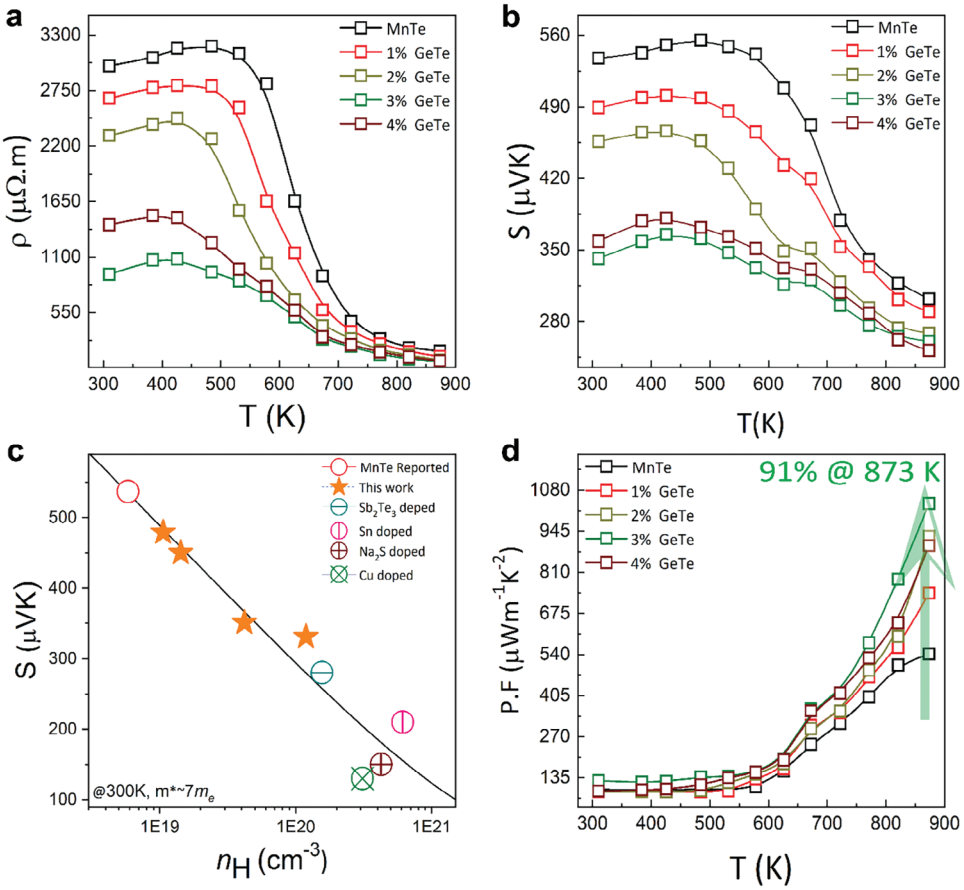

Figure 4. Electrical transport properties of MnTe + x mol.% GeTe ($0 \le x \le 4$) samples. a) Resistivities (ρ); b) Seebeck coefficients (S); c) Pisarenko relation between the S and n_H; d) power factors (P.F).

have further reduced the lattice thermal conductivity. This approach suggests that originated precipitates in the matrix can lead to sufficient phonon scattering and hence reduce κ_l as compared to the 1.5 at% Sb_2Te_3 added MnTe.[2] The lattice thermal conductivity (κ_l) was determined using the Callaway model (Figure 5c; Table S2, Supporting Information), considering various phonon scattering centers such as U (umklapp-process), EP (electrons-phonons), GB (grain boundaries), and NP (nanoparticles) in the GeTe added MnTe sample, in comparison to the MnTe matrix (U + EP + GB). The results clearly demonstrate that the presence of GeTe secondary phases leads to a substantial reduction in κ_l, with a particularly pronounced effect at high temperature (873K) within the Deby-cutoff phonon frequency range (Figure 5d).

Benefiting from the well-organized strategy, the electrical and thermal transport properties of the MnTe compound have tactfully decoupled with the introduction of GeTe. The electrical resistivity reduces sharply with increased carrier concentration in the MnTe + x mol.% GeTe ($0 \le x \le 4$) samples, and thus the power factor increases by ≈91% for the MnTe + 3 mol.% GeTe sample in comparison to the pristine MnTe. However, a variety of defects results in the strengthening of phonons scattering in MnTe + 3 mol.% GeTe sample at elevated temperatures especially. Thus, **Figure** 6a illustrates that the MnTe + x mol.% GeTe materials exhibit a relatively high average ZT_{ave} value of 0.9 within the medium-temperature range of 770 K − 873 K. Moreover, the resultant ZT increases with the increase of GeTe content as presented in Figure 6b. Here, a maximum ZT reaches ≈1.2 for MnTe + x mol.% GeTe (x = 3%) sample at 873 K, which suggests that GeTe might be a convincible route to explore the other Mn-based chalcogenides as obvious from the other reports (see Figure 6c).

3. Conclusion

In summary, a series of MnTe + x mol.% GeTe ($0 \le x \le 4$) compounds have been prepared to explore the influence of GeTe doping on the thermoelectric properties of the MnTe compound. This study demonstrates a concurrent optimization of electrical and thermal transport properties of MnTe + 3 mol.% GeTe sample in the presence of stimulated carrier density and some lamellar defects with other nano-inclusions at elevated temperatures. On one hand, the enhanced hole concentration from the Ge deficiency increases the electrical performance and thus power factor to ~1036 mW m^{-1} K^{-2} at 873 K for MnTe + 3 mol.% GeTe sample. On the other hand, secondary phases as well as the originated defects result in a strong phonon scattering and hence a suppressed lattice thermal conductivity ≈0.73 W m^{-1} K^{-1} in MnTe + 3 mol.% GeTe sample. Ultimately a ZT reaches ≈1.2 for MnTe + x mol.% GeTe (x = 3%) sample at 873 K, which increases ≈93% in comparison to the pristine MnTe.

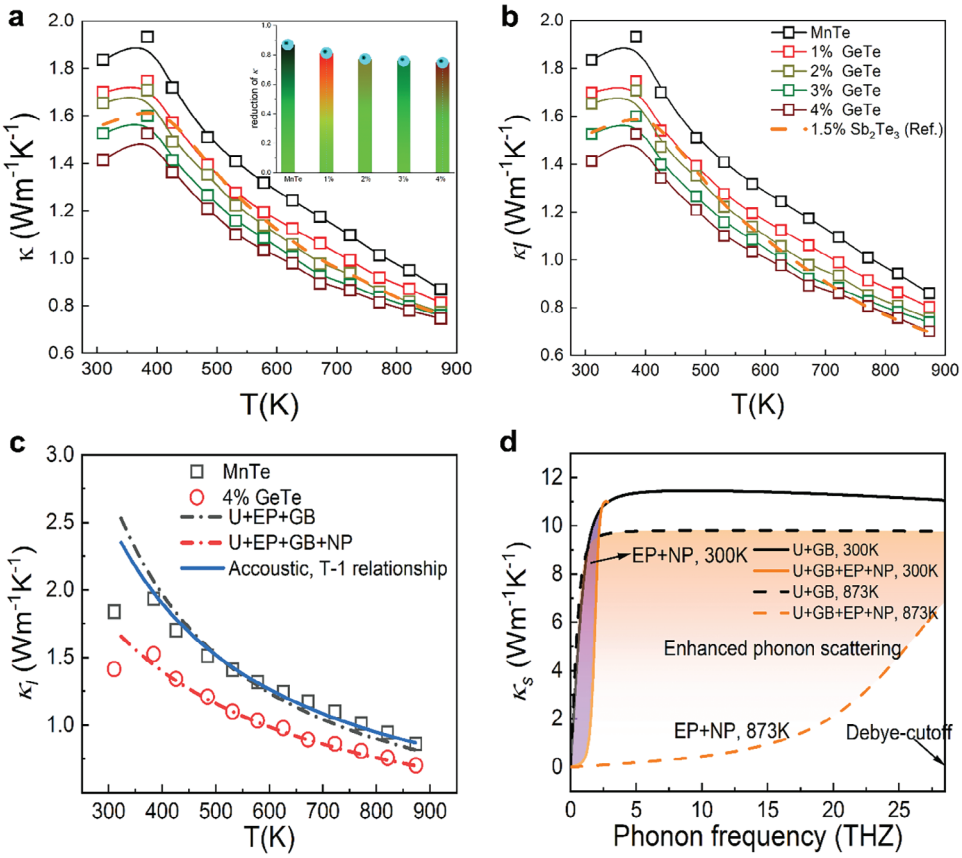

Figure 5. Temperature-dependent thermal transport properties of MnTe + *x* mol.% GeTe ($0 \le x \le 4$). a) Total thermal conductivities; b) lattice thermal conductivities; c) the lattice thermal conductivity κ_l for MnTe matrix and composited sample compared with the calculated κ_l by using the Callaway model; d) the theoretic spectral lattice thermal conductivity κ_s with phonon scattering centers.

4. Experimental Section

Synthesis of Materials: The pristine MnTe ingot was prepared by melting high-purity commercial powder of Mn and Te (99.99%, Aladdin, China) in a vacuum-sealed (10^{-3} Pa) quartz tube at 1473 K for 2 days. Similarly, a pristine GeTe ingot was prepared by melting and annealing high-purity commercial powder of Ge and Te (99.99%, Aladdin, China) in a vacuum-sealed (10^{-3} Pa) quartz tube at 973 K for 2 days. Further, the MnTe and GeTe ingots were pulverized in an agate mortar separately and then the powder was mixed within the ratios of MnTe + *x* mol.% GeTe ($0 \le x \le 4$) and densified using hot-press at 873 K under a pressure of ≈90 MPa for 2 h in Ar atmosphere as shown schematically in Figure 1a.

Measurement and Characterization: The composition, morphology, and crystal structure were characterized by means of X-ray diffraction and transmission electron microscopy (TEM) JEOL JEM−2100dispersive equipped with energy dispersive X-ray (EDX) analysis. Seebeck coefficient

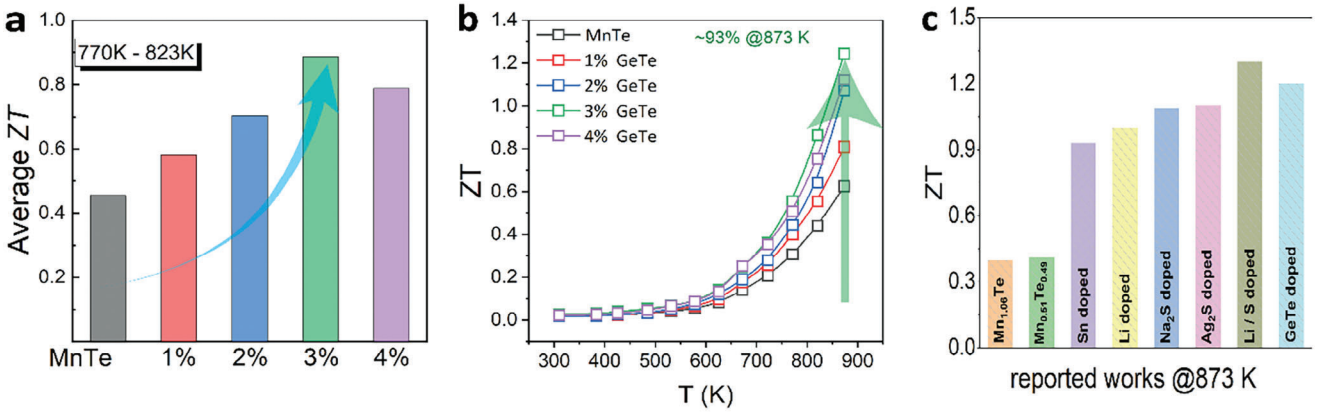

Figure 6. a) Average ZT values of this work in the temperature range 773 K – 873 K; b) Thermoelectric figure of merit of MnTe + *x* mol.% GeTe ($x = 0$, 1, 2, 3, 4); c) comparison of the figure of merit of MnTe + 3 mol.% GeTe sample with the other reported in.[2,3,6,21,22,38,67]

and electrical resistivity for all the samples were measured with a custom-designed thermoelectric measurement system (Namicro–III), and electric transport properties were characterized by a Hall effect measurement system (HMS 5500) with a Van der Pauw electrode configuration. The thermal conductivities of the samples were measured based on the equation $\kappa = DCpd$,[56] where the thermal diffusivity (d) was measured by the laser flashing method (LFA–427, NETZSCH) in the N_2 atmosphere (Figure S1, Supporting Information), and the density (D) was estimated by the Archimedes' method. Further, the specific heats (C*p*) were taken from the measured reference value (Figure S2, Supporting Information).[56]

Supporting Information

Supporting Information is available from the Wiley Online Library or from the author.

Acknowledgements

This work was supported by the National Natural Science Foundation of China under Grant Nos. 92163211, 52002137, 51872102, and 51802070 and Graduates' Innovation Fund, Huazhong University of Science and Technology under Grant No. 2020yjsCXCY022. The authors acknowledge the support from the Guangdong–Hong Kong–Macao Joint Laboratory for Photonic-Thermal-Electrical Energy Materials and Devices (GDSTC No. 2019B121205001). A.B. thanks to the PolyU Postdoc Matching Fund support (1-W23Z).

Conflict of Interest

The authors declare no conflict of interest.

Data Availability Statement

The data that support the findings of this study are available from the corresponding author upon reasonable request.

Keywords

carrier concentration, GeTe, microstructure, MnTe, thermoelectric

Received: November 19, 2023
Revised: January 27, 2024
Published online: March 19, 2024

[1] J. J. Banewicz, R. F. Heidelberg, A. H. Luxem, *J Phys Chem A.* **1961**, *65*, 615.
[2] A. Basit, J. Yang, Q. Jiang, J. Xin, X. Li, S. Li, S. Li, Q. Long, *J Mater Chem.* **2018**, *6*, 23473.
[3] A. Basit, J. Yang, Q. Jiang, Z. Zhou, J. Xin, X. Li, S. Li, *J. Alloys Compd.* **2019**, *777*, 968.
[4] J. D. Efrem, P. A. Bhobe, K. R. Priolkar, A. Das, S. K. Paranjpe, R. B. Prabhu, P. R. Sarode, *J. Magn. Magn. Mater.* **2005**, *285*, 267.
[5] D. D. Sante, P. Barone, R. Bertacco, S. Picozzi, *Adv. Mater.* **2013**, *25*, 509.
[6] J. Dong, J. Pei, K. Hayashi, W. Saito, H. Li, B. Cai, Y. Miyazaki, J. L. Feng, *J Mater.* **2021**, *7*, 577.
[7] J. Dong, F. Sun, H. Tang, K. Hayashi, H. Li, P. Shang, Y. Miyazaki, J. L. Feng, *ACS Appl Mater Interfaces.* **2019**, *11*, 28221.
[8] J. Dong, C. Wu, J. Pei, F. Sun, Y. Pan, B. P. Zhang, H. Tang, J. L. Feng, *J Mater Chem.* **2018**, *6*, 4265.
[9] F. Liangwei, Y. Meijie, D. Wu, W. Li, D. Feng, L. Huang, J. He, *Energy Environ. Sci.* **2017**, *10*, 2030.
[10] R. He, H. Zhu, J. Sun, J. Mao, H. Reith, S. Chen, G. Schierning, K. Nielsch, Z. Ren, *Mater. Today Phys.* **2017**, *1*, 24.
[11] B. Hennion, W. Szuszkiewicz, E. Dynowska, E. Janik, T. Wojtowicz, *Phys Rev B.* **2002**, *66*, 224426.
[12] J. P. Heremans, V. Jovovic, E. S. Toberer, A. Saramat, K. Kurosaki, A. Charoenphakdee, S. Yamanaka, G. J. Snyder, *Stem Cells Int.* **2008**, *321*, 554.
[13] M. Hong, Z. G. Chen, L. Yang, Y. C. Zou, M. S. Dargusch, H. Wang, J. Zou, *Adv. Mater.* **2018**, *30*, 1705942.
[14] M. Hong, Y. Wang, W. Liu, S. Matsumura, H. Wang, J. Zou, Z. G. Chen, *Adv. Energy Mater.* **2018**, *8*, 1801837.
[15] K. F. Hsu, S. Loo, F. Guo, W. Chen, J. S. Dyck, C. Uher, T. Hogan, E. K. Polychroniadis, M. G. Kanatzidis, *Science.* **2004**, *303*, 818.
[16] B. Huang, P. Zhai, X. Yang, G. Li, *J. Electron. Mater.* **2017**, *46*, 2797.
[17] J. Hwang, M. Lee, B. K. Yu, M. K. Han, W. Kim, J. Kim, R. A. Rahal, H. Wang, S. Acharya, J. Kim, *J Mater Chem.* **2021**, *9*, 14851.
[18] B. Jiang, Y. Yu, J. Cui, X. Liu, L. Xie, J. Liao, Q. Zhang, Y. Huang, S. Ning, B. Jia, *Science.* **2021**, *371*, 830.
[19] Y. Jiang, J. Dong, H. L. Zhuang, J. Yu, B. Su, H. Li, J. Pei, F. H. Sun, M. Zhou, H. Hu, *Nat. Commun.* **2022**, *13*, 6087.
[20] S. M. Kauzlarich, S. R. Brown, G. J. Snyder, *Dalton Trans.* **2007**, *107*, 2099.
[21] B. Kim, I. Kim, B. Min, O. Minwook, S. Park, H. Lee, *Electron. Mater. Lett.* **2013**, *9*, 477.
[22] X. She, X. Su, H. Xie, J. Fu, Y. Yan, W. Liu, P. Poudeu, X. Tang, *ACS Appl Mater Interfaces.* **2018**, *30*, 25519.
[23] K. Koumoto, I. Terasaki, R. Funahashi, *MRS Bull.* **2006**, *31*, 206.
[24] L. Meng, D. L. Cortie, J. Liu, Y. Dehong, S. K. Islam, L. Zhao, D. R. Mitchell, R. A. Mole, M. B. Cortie, D. Shixue, *Nano Energy.* **2018**, *53*, 993.
[25] L. Weixin, Y. Luo, Y. Zheng, D. Chengfeng, Q. Liang, B. Zhu, L. Zhao, *J Mater Sci.* **2018**, *29*, 4732.
[26] Y. B. Li, Y. Q. Zhang, N. K. Sun, Q. Zhang, D. Li, J. Li, Z. D. Zhang, *Phys Rev B.* **2005**, *72*, 193308.
[27] D. Liu, B. Qin, L. D. Zhao, *Materials Lab.* **2022**, *1*, 220006.
[28] Z. Liu, W. Gao, F. Guo, W. Cai, Q. Zhang, J. Sui, *Materials Lab.* **2022**, *1*, 220003.
[29] Y. Luo, J. Wang, J. Yang, D. Mao, J. Cui, B. Jia, X. Liu, K. Nielsch, X. Xu, J. He, *Energy Environ. Sci.* **2023**, *16*, 3743.
[30] Y. Luo, S. Cai, S. Hao, F. Pielnhofer, I. Hadar, Z. Z. Luo, J. Xu, C. Wolverton, V. P. Dravid, A. Pfitzner, *Joule.* **2020**, *4*, 159.
[31] Y. Luo, S. Cai, X. Hua, H. Chen, Q. Liang, C. Du, Y. Zheng, J. Shen, J. Xu, C. Wolverton, *Adv. Energy Mater.* **2019**, *9*, 1803072.
[32] Y. Luo, T. Xu, Z. Ma, D. Zhang, Z. Guo, Q. Jiang, J. Yang, Q. Yan, M. G. Kanatzidis, *J. Am. Chem. Soc.* **2021**, *143*, 13990.
[33] Y. Luo, J. Yang, Q. Jiang, W. Li, Y. Xiao, L. Fu, D. Zhang, Z. Zhou, Y. Cheng, *Nano Energy.* **2015**, *18*, 37.
[34] Z. Ma, T. Xu, W. Li, Y. Cheng, J. Li, D. Zhang, Q. Jiang, Y. Luo, J. Yang, *Adv. Funct. Mater.* **2021**, *31*, 2103197.
[35] G. S. Nolas, J. Poon, M. Kanatzidis, *MRS Bull.* **2006**, *31*, 199.
[36] S. Perumal, S. Roychowdhury, D. S. Negi, R. Datta, K. Biswas, *Chem. Mater.* **2015**, *27*, 7171.
[37] Y. Ren, Q. Jiang, J. Yang, Y. Luo, D. Zhang, Y. Cheng, Z. Zhou, *J Mater.* **2016**, *2*, 172.
[38] Y. Ren, J. Yang, Q. Jiang, D. Zhang, Z. Zhou, X. Li, J. Xin, X. He, *J Mater Chem.* **2017**, *5*, 5076.
[39] C. M. Rost, E. Sachet, T. Borman, A. Moballegh, E. C. Dickey, D. Hou, J. L. Jones, S. Curtarolo, J. P. Maria, *Nat. Commun.* **2015**, *6*, 8485.
[40] S. Roychowdhury, T. Ghosh, R. Arora, M. Samanta, L. Xie, N. K. Singh, A. Soni, J. He, U. V. Waghmare, K. Biswas, *Science.* **2021**, *371*, 722.

[41] S. Sakurada, N. Shutoh, *Appl. Phys. Lett.* **2005**, *86*, 082105.
[42] L. M. Sandratskii, R. F. Egorov, A. A. Berdyshev, *Phys. Status Solidi B.* **1981**, *104*, 103.
[43] U. Saparamadu, J. D. Boor, J. Mao, S. Song, F. Tian, W. Liu, Q. Zhang, Z. Ren, *Acta Mater.* **2017**, *141*, 154.
[44] X. Shi, A. Wu, T. Feng, K. Zheng, W. Liu, Q. Sun, M. Hong, S. T. Pantelides, Z. G. Chen, J. Zou, *Adv. Energy Mater.* **2019**, *9*, 1803242.
[45] G. J. Snyder, E. S. Toberer, *Nat. Mater.* **2008**, *7*, 105.
[46] J. R. Sootsman, D. Y. Chung, M. G. Kanatzidis, *Angew. Chem., Int. Ed.* **2009**, *48*, 8616.
[47] W. Szuszkiewicz, E. Dynowska, B. Witkowska, B. Hennion, *Phys Rev B.* **2006**, *73*, 104403.
[48] G. Tan, F. Shi, S. Hao, L. D. Zhao, H. Chi, X. Zhang, C. Uher, C. Wolverton, V. P. Dravid, M. G. Kanatzidis, *Nat. Commun.* **2016**, *7*, 12167.
[49] G. Tang, W. Wei, J. Zhang, Y. Li, X. Wang, G. Xu, C. Chang, Z. Wang, Y. Du, L. D. Zhao, *J. Am. Chem. Soc.* **2016**, *138*, 13647.
[50] X. Q. Tran, M. Hong, H. Maeno, Y. Kawami, T. Toriyama, K. Jack, Z. G. Chen, J. Zou, S. Matsumura, M. S. Dargusch, *Acta Mater.* **2019**, *165*, 327.
[51] C. Uher, *Semicond. Semimet.* **2001**, *69*, 139.
[52] C. Wang, Q. Ma, H. Xue, Q. Wang, P. Luo, J. Yang, W. Zhang, J. Luo, *ACS Appl. Energy Mater.* **2020**, *3*, 11015.
[53] W. Wei, C. Chang, T. Yang, J. Liu, H. Tang, J. Zhang, Y. Li, F. Xu, Z. Zhang, J. F. Li, *J. Am. Chem. Soc.* **2018**, *140*, 499.
[54] D. Wu, L. D. Zhao, S. Hao, Q. Jiang, F. Zheng, J. W. Doak, H. Wu, H. Chi, Y. Gelbstein, C. Uher, *J. Am. Chem. Soc.* **2014**, *136*, 11412.
[55] H. Wu, J. Carrete, Z. Zhang, Y. Qu, X. Shen, Z. Wang, L. D. Zhao, J. He, *NPG Asia Mater.* **2014**, *6*, e108.
[56] W. Xie, S. Populoh, K. Gałązka, X. Xiao, L. Sagarna, Y. Liu, M. Trottmann, J. He, A. Weidenkaff, *J. Appl. Phys.* **2014**, *115*, 103707.
[57] J. Xin, J. Yang, Q. Jiang, S. Li, A. Basit, H. Hu, Q. Long, S. Li, X. Li, *Nano Energy.* **2019**, *57*, 703.
[58] W. Xiong, Z. Wang, X. Zhang, C. Wang, L. Yin, Y. Gong, Q. Zhang, S. Li, Q. Liu, P. Wang, *Small.* **2023**, *19*, 2206058.
[59] Y. Xu, W. Li, C. Wang, Z. Chen, Y. Wu, X. Zhang, J. Li, S. Lin, Y. Chen, Y. Pei, *J Mater.* **2018**, *4*, 215.
[60] Y. Xu, W. Li, C. Wang, J. Li, Z. Chen, S. Lin, Y. Chen, Y. Pei, *J Mater Chem.* **2017**, *5*, 19143.
[61] D. Yang, X. Su, J. Li, H. Bai, S. Wang, Z. Li, H. Tang, K. Tang, T. Luo, Y. Yan, *Adv. Mater.* **2020**, *32*, 2003730.
[62] F. Zhang, D. Wu, J. He, *Materials Lab.* **2022**, *1*, 220012.
[63] J. Zhang, D. Wu, D. He, D. Feng, M. Yin, X. Qin, J. He, *Adv. Mater.* **2017**, *29*, 1703148.
[64] K. Zhao, A. B. Blichfeld, H. Chen, Q. Song, T. Zhang, C. Zhu, D. Ren, R. Hanus, P. Qiu, B. B. Iversen, *Chem. Mater.* **2017**, *29*, 6367.
[65] L. D. Zhao, J. He, C. Wu, T. P. Hogan, X. Zhou, C. Uher, V. P. Dravid, M. G. Kanatzidis, *J. Am. Chem. Soc.* **2012**, *134*, 7902.
[66] S. Zhao, Z. Li, *Materials Lab.* **2022**, *1*, 220035.
[67] Y. Zheng, T. Lu, M. M. Polash, M. Rasoulianboroujeni, N. Liu, M. E. Manley, Y. Deng, P. J. Sun, X. L. Chen, R. P. Hermann, *Sci. Adv.* **2019**, *5*, eaat9461.
[68] S. Zulkifal, Z. Wang, X. Zhang, S. Siddique, Y. Yu, C. Wang, Y. Gong, S. Li, D. Li, Y. Zhang, *Adv. Sci.* **2023**, *10*, 2206342.